Electronic and Structural Fingerprints of Charge-Density-Wave Excitations in Extreme Ultraviolet Transient Absorption Spectroscopy

Tobias Heinrich,[1] Hung-Tzu Chang,[1,2] Sergey Zayko,[1,5] Kai Rossnagel,[3,4] Murat Sivis,[1,5] and Claus Ropers[1,5,*]

[1]*Max Planck Institute for Multidisciplinary Sciences, 37077 Göttingen, Germany*
[2]*Department of Chemistry, University of California, Berkeley, California 94720, USA*
[3]*Institute of Experimental and Applied Physics, Kiel University, 24098 Kiel, Germany*
[4]*Ruprecht Haensel Laboratory, Deutsches Elektronen-Synchrotron DESY, 22607 Hamburg, Germany*
[5]*4th Physical Institute—Solids and Nanostructures, University of Göttingen, 37077 Göttingen, Germany*

(Received 17 October 2022; revised 22 February 2023; accepted 4 April 2023; published 7 June 2023)

Femtosecond core-level transient absorption spectroscopy is utilized to investigate photoinduced dynamics of the charge density wave in $1T$-$TiSe_2$ at the Ti $M_{2,3}$ edge (32–50 eV). Photoexcited carriers and phonons are found to primarily induce spectral redshifts of core-level excitations, and a carrier relaxation time and phonon heating time of approximately 360 fs and 1.0 ps are extracted, respectively. Pronounced oscillations in delay-dependent absorption spectra are assigned to coherent excitations of the optical A_{1g} phonon (6.0 THz) and the A_{1g}^* charge density wave amplitude mode (3.3 THz). By comparing the measured spectra with time-dependent density functional theory simulations, we determine the directions of the momentary atomic displacements of both coherent modes and estimate their amplitudes. Interestingly, the spectral fingerprint of the amplitude mode can be associated with many-body electron screening, strengthening the importance of electron-electron and simultaneous electron-phonon interaction for the stability of the charge density wave. In addition, we find that 10% and 13% of the absorbed energy is stored in the A_{1g} and A_{1g}^* coherent modes, respectively. This work presents a first look on charge density wave excitations with tabletop core-level transient absorption spectroscopy, enabling simultaneous access to electronic and lattice excitation and relaxation.

DOI: 10.1103/PhysRevX.13.021033

Subject Areas: Condensed Matter Physics, Optics, Strongly Correlated Materials

I. INTRODUCTION

Electronic processes in quantum materials including superconductors, Mott insulators, and charge density wave (CDW) compounds encompass a wide range of phenomena with collective excitations involving coupled electronic, vibrational, and spin dynamics [1–4]. The layered transition metal dichalcogenide $1T$-$TiSe_2$ features CDW formation below a critical temperature (T_c) of 200 K [5], linked to a periodic lattice distortion (PLD) in the form of a $2 \times 2 \times 2$ supercell [6], shown in Fig. 1(a). Various mechanisms, including Jahn-Teller effects and exciton condensation, have been proposed to explain the CDW formation, yet the exact mechanism of CDW formation is still unclear and subject of many studies [7–14]. Recent experiments on ultrafast nonthermal melting of the CDW in $1T$-$TiSe_2$ suggest that the electronic and vibrational degrees of freedom are strongly coupled in the CDW quenching process [15–27], and different timescales of the loss of electronic and structural orders have been observed [28,29].

To understand such complex photophysical phenomena, simultaneous probing of the electronic and lattice subsystems in a single experiment is highly beneficial, as it allows for a study of both degrees of freedom at identical experimental conditions. Core-level transient absorption spectroscopy, in which the sample is pumped with a femtosecond optical pulse and subsequently probed by an extreme ultraviolet (XUV) pulse, is ideally suited for this purpose. This method has been successfully utilized to simultaneously observe the decay of photoexcited carriers and coherent phonons in $MoTe_2$ [31] and to disentangle the intricate electron phonon dynamics in graphite [32]. However, up to now, XUV radiation has not been used to study excitations of CDWs. In this work, we apply core-level spectroscopy at the Ti $M_{2,3}$ edge (32–50 eV) to investigate photoinduced excitations of the CDW in $1T$-$TiSe_2$. Thereby, we analyze the transient absorption by comparing with *ab initio* simulations conducted with time-dependent density functional theory (TDDFT).

*Corresponding author.
claus.ropers@mpinat.mpg.de

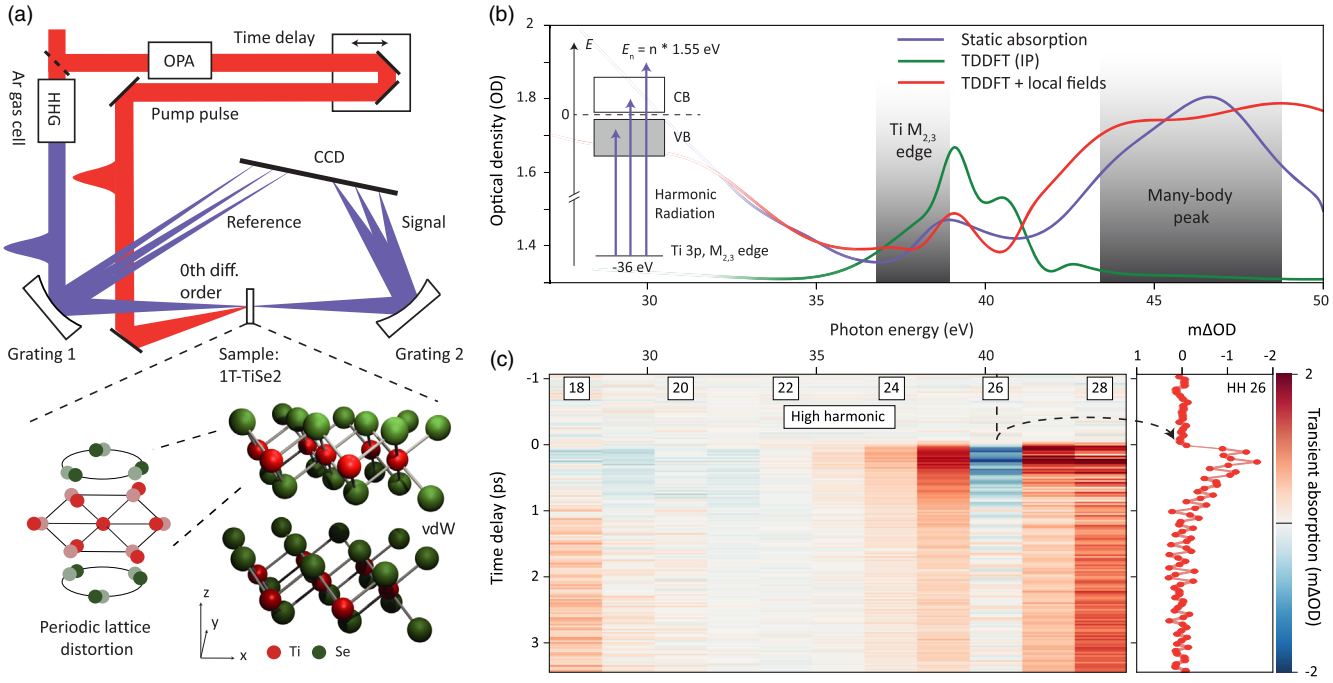

FIG. 1. (a) Setup for extreme ultraviolet (XUV) transient absorption spectroscopy, where fluctuations of the high-harmonic generation (HHG) source are tracked with a reference spectrum for noise reduction. The 1T-$TiSe_2$ specimen consists of layers held by van der Waals (vdW) forces and shows a charge density wave with an associated periodic lattice distortion. (b) Static absorption spectrum recorded with a continuous HHG source (purple line) [30]. Time-dependent density functional theory (TDDFT) calculations under independent particle (IP) approximation (green line) and with the inclusion of local field effects (red line). The latter qualitatively reproduces the Ti $M_{2,3}$ edge (approximately 36.5 eV) as well as the many-body absorption peak at 42–49 eV. Inset: Titanium M edge originating from transitions of the Ti 3p orbital to empty states in the valence (VB) and conduction band (CB). (c) Exemplary transient absorption spectrum recorded with discrete harmonics spaced by 1.55 eV. Relative changes to an unpumped sample are shown for various time delays of the pump pulse.

We distinguish the electronic and phonon contributions to the core-level transient absorption spectra, extract the timescales of hot electron cooling and phonon heating, separate contributions from different coherent phonon modes by spectral fingerprints, and identify their corresponding atomic displacements, excitation efficiency, and dephasing times.

II. RESULTS

The core-level transient absorption experiment is conducted with a 65-nm-thick 1T-$TiSe_2$ flake on a 30-nm-thick silicon membrane (Appendix A) at a temperature of 110 K. Details of the experimental setup [Fig. 1(a)] are described in Appendix B and Ref. [33]. In brief, the sample is optically excited by a 40-fs laser pulse centered at 2-μm wavelength and probed by a time-delayed XUV beam covering the spectral range of 25–50 eV. The XUV radiation is produced through high-harmonic generation (HHG) driven by 35-fs-long laser pulses (800 nm center wavelength) and their second harmonic in an Ar-filled gas cell. The two-color field creates both even and odd harmonics of the fundamental driving beam centered at 1.55 eV. The absorption of the XUV radiation in the investigated spectral range is dominated by transitions of the Ti 3p electrons into the valence shell [Fig. 1(b)]. The pump-induced change of the XUV absorbance is defined as the difference between the absorbance [optical density (OD)] with and without optical excitation ($\Delta\mathrm{OD} = \mathrm{OD}_{\mathrm{pumped}} - \mathrm{OD}_{\mathrm{unpumped}}$). An additional reference spectrum of the harmonic source is simultaneously collected for noise suppression, which provides an improved sensitivity beyond 10^{-4} OD [33] and enables the detection of subtle CDW dynamics, as found in 1T-$TiSe_2$ at low pump fluences. More specifically, the investigation of CDW excitations is largely restricted to fluences below the threshold for nonthermal CDW melting [29].

Figure 1(b) displays a static absorption spectrum of 1T-$TiSe_2$ (purple line), recorded with a spectrally continuous source [30]. Here, the Ti $M_{2,3}$ edge exhibits a small peak with an onset at approximately 36.5 eV and another strong absorption peak centered at about 47 eV. The absorption below the edge (< 36.5 eV) results from excitations of electrons within the valence shell, which are dominated by the bulk plasmon peak centered at 20 eV [34]. This contribution to the absorption decreases with increasing photon energy such that only the tail is seen in

the XUV spectra below 36 eV. As this spectral region does not involve excitations of core-level states, it is expected to behave differently from the M-edge spectrum at energies larger than 36 eV. To understand the Ti $M_{2,3}$-edge transitions, we compare the measured static spectrum with TDDFT simulations (Appendix E) in the linear response theory under random phase approximation. The simulated transitions within the independent particle (IP) approximation [Fig. 1(b), green line] overlap only with the approximately 39 eV small peak in the empirical spectrum, whereas the strong peak at approximately 47 eV is absent. Calculations including local field effects [Fig. 1(b), red line] [35], where many-body interactions in electronic excitations are partially accounted for, qualitatively reproduce the empirical spectrum. This suggests that the small peak at the onset of the Ti $M_{2,3}$ edge (36.5 eV) mainly constitutes single-particle excitations from the Ti $3p$ orbitals to the conduction band. In addition, the strong peak at approximately 47 eV can be identified as a giant resonance [36,37] comprising transitions from the Ti $3p$ levels to the conduction band, accompanied by valence-shell excitations from below to above the Fermi level through configuration interactions. Here, the local screening to the core electron results in a collective resonance above the core-level edge in addition to the single-electron transitions. In transition metals and transition-metal dichalcogenides, it has been found that many-body resonance is highly sensitive to the local charge density around the excited atom [38,39]. To this end, the spectral region of the giant resonance at approximately 47 eV is ideally suited to study the charge density wave dynamics in $1T$-$TiSe_2$.

The photoinduced dynamics in $1T$-$TiSe_2$ are tracked by recording XUV absorption spectra as a function of the pump-probe time delay τ [Fig. 1(c)]. Because of the discrete spectrum of the harmonic source (Appendix B) and the weak pump-induced signals ($< 10^{-3}$ OD), the spectra are binned to the center of each harmonic peak, separated by the photon energy of the fundamental driving laser (1.55 eV). At pump-probe overlap ($\tau \approx 0$), the absorbance decreases at energies below 35 eV. An increase in absorbance is observed in both the Ti $M_{2,3}$ near-edge region (35–39 eV) and at the onset of the many-body giant resonance (42–45 eV). In between the tail of the lower-energy peak of the Ti $M_{2,3}$ edge (39 eV) and the onset of the giant resonance (42 eV), a decrease in absorbance is found. At long time delays ($\tau > 3$ ps), an absorbance increase is seen across the entire spectrum. At time delays up to about 3 ps, oscillations in transient absorption signals are evident from the 26th to the 31st harmonic [Fig. 1(c), right]. In the following sections, we analyze the transient absorption signals at pump-probe overlap and > 3 ps time delay (Sec. II A), discuss the origin of the oscillations (Sec. II B), and extract the timescales of the underlying physical processes.

A. Hot electron dynamics and lattice heating

Transient absorption signals at $\tau = 50$ fs and 3 ps are plotted in Fig. 2(a) (dots) for a pump fluence of 0.66 mJ/cm^2. As the energy transfer from the electrons to the lattice typically occurs on the hundreds of femtoseconds to picosecond timescale [23,27], photoexcited carriers are expected to be the main contributor to the transient absorption signal at 50-fs delay. This time delay is intentionally chosen to show only the effects of the excited electron system shortly after the laser pulse excitation. In many materials, photoexcited carriers contribute to a positive core-level transient absorption signal below the edge and a negative signal above the edge due to holes and electrons below and above the Fermi level, respectively [31,40–44]. However, at the onset of the Ti $M_{2,3}$ edge, the transient absorption signal exhibits an increase with energy, contrary to the expected signal contribution from electronic state blocking. This can be explained by significant many-body effects affecting the core-level transitions [30,38,45].

Previous studies observe an electron-temperature-induced derivative absorption feature in a variety of materials [31,38,43,45–47] which is assigned to a band gap renormalization in semiconductors and chemical potential changes plus changes in electronic screening in metals. Both effects lead to a shift of the empty final states, which are overlapped by a broadening of the absorption edge. In addition, the changed electronic screening may also shift the energy of the core level [48]. In a complex semimetal like $1T$-$TiSe_2$, it is nontrivial to assign a specific microscopic mechanism, but all mentioned effects are well described by a spectral shift plus some broadening of the static absorption spectrum [45]. We apply such an analysis by first separating the spectrum into two regions: the region containing the Ti $M_{2,3}$-edge transitions (> 36.5 eV) and the region mainly contributed by the tail of the bulk plasmon excitation [< 36.5 eV; cf. Fig. 1(b)], which does not include a core-level excitation and is, therefore, not further discussed in this work. By applying redshifts of 1.5 and 8 meV to the static absorption spectrum below and above 36.5 eV, respectively, the resulting spectrum shows reasonable agreement with the empirical transient absorption data [Fig. 2(a), red line and dots]. We do not observe a pronounced broadening of the Ti M edge in $1T$-$TiSe_2$. At photon energies of > 44 eV, the energy cutoff of our HHG light source is reached, which leads to higher noise levels overshadowing the signal. Therefore, we cannot resolve the small redshift in this spectral region that is predicted by the simulations.

We compare the measured transient absorption spectrum at 50 fs with TDDFT simulations to explore whether a hot (quasithermalized) electronic population is consistent with the observed absorption changes. Figure 2(a) (green dashed line) shows the difference between the core-level absorption spectrum simulated for an electronic temperature of 1000 and 110 K. Here, the electron temperature is adjusted

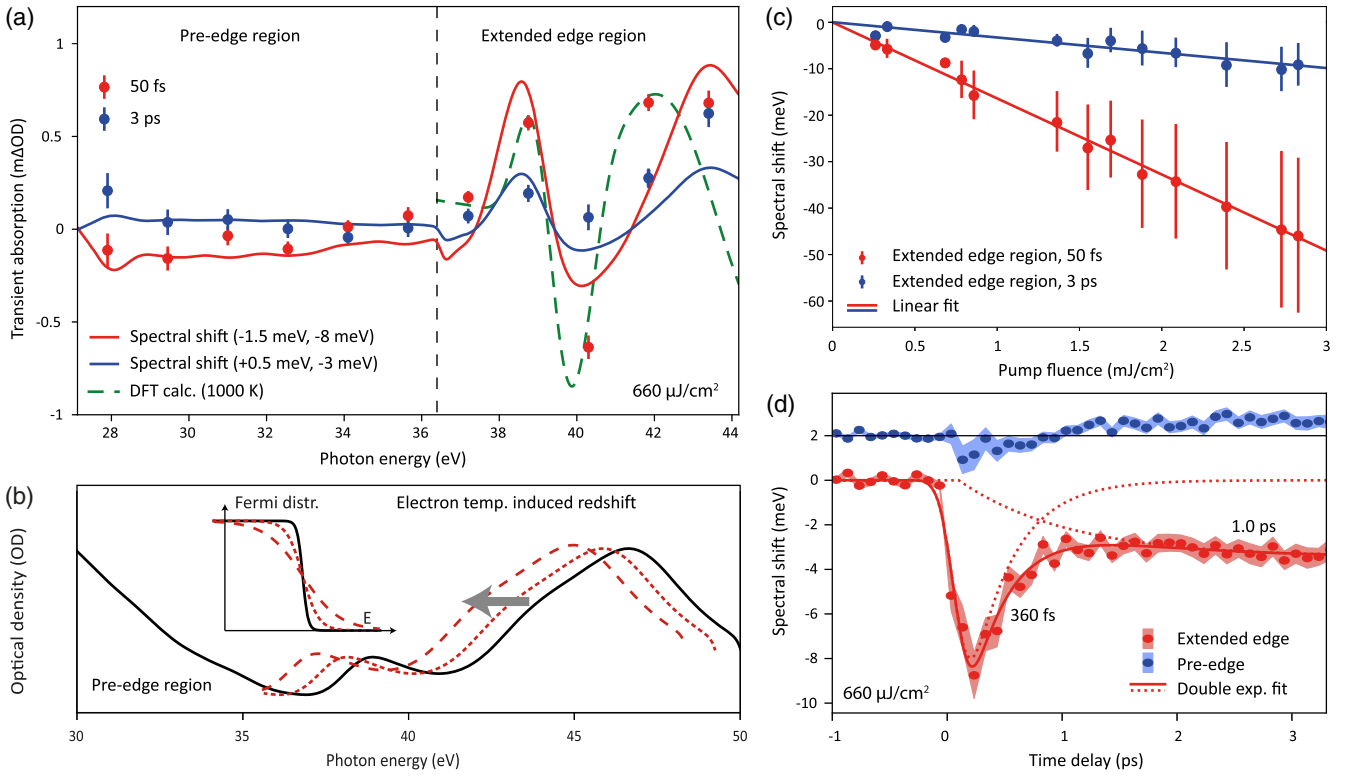

FIG. 2. (a) Transient absorption spectra. The energy-dependent response can be modeled with selective spectral shifts of the static spectrum [Fig. 1(b)]. To this end, the spectral range is separated into the pre-edge (< 36.5 eV) and extended edge (> 36.5 eV) regions. Complementary TDDFT calculation for elevated electron temperature (green dashed line) shows a similar spectral change. The spectral width of the harmonics is < 250 meV. (b) Schematic spectral changes induced by electronic heating. (c) Fluence dependence of the extended edge shifts, showing a linear scaling in support of thermal mechanisms. (d) Temporal dynamics of spectral shifts in the pre-edge and extended edge region. A double-exponential fit extracts electronic excitation decaying on approximately 360 fs and contributions of the phonon bath that emerge on the picosecond timescale.

by the Fermi distribution in the calculation, and the calculation also accounts for the electron-temperature-induced band changes described in the previous paragraph. According to fluence-dependent measurements [Fig. 2(c)], the behavior of the spectral redshift does not differ below and above the thermal CDW transition threshold. Therefore, we use the normal state of 1*T*-$TiSe_2$ instead of the PLD supercell, as the CDW is not expected to significantly influence the spectral signature of excited electrons. The fluence-dependent measurements are further discussed in a later paragraph. A temperature of 1000 K corresponds to the estimated electron temperature at the pump fluence of 0.66 mJ/cm^2, calculated in the free electron gas model. The simulation shows good agreement with the experimental spectrum, suggesting that at 50 fs an excited electronic population leads to a redshift qualitatively shown in Fig. 2(b). Notably, the TDDFT calculation is in even better agreement with the data compared to the simplified spectral shift model.

In contrast to the dominance of photoexcited electrons in the transient absorption spectrum at 50-fs time delay, the spectrum at 3-ps delay is expected to be dominated by the heated phonon bath. An increase in the lattice temperature can influence the XUV spectrum by thermal expansion [43,49] and electron-phonon coupling, which was previously observed to shrink the band gap and also lead to a derivative-shaped absorption feature [31,40,43,49]. The effect has been analyzed in comparison to the Debye-Waller effect from electron diffraction data [43], and it was found that at large time delays the near edge spectral changes can be assigned to the lattice temperature. In this study, we estimate a lattice and electron temperature of 30 K at equilibrium using the pump fluence (see Appendix C). At this temperature, the expected contribution from the electronic temperature increase is only 0.3 meV and can be neglected. Thus, the empirical transient absorption spectrum at 3 ps can be attributed to lattice heating and approximated by a much larger redshift of the static absorption spectrum. Figure 2(a) (blue line and dots) shows that the transient absorption below 36.5 eV is diminished to almost zero, while the spectrum above 36.5 eV can be qualitatively described by a 3-meV redshifted static absorption spectrum. The agreement between the empirical data and energy-shifted static

spectrum degrades in the > 40-eV region. This may be explained by the different response to photoexcitations between the Ti $M_{2,3}$-edge onset, which is mainly due to one-body core-level excitations, and the giant resonance at > 42 eV, where many-body effects dominate. The absorption in the > 40 eV region is therefore expected to be influenced by both mechanisms. As the fitting incorporates only one spectral shift parameter, the behavior of the transient absorption signal cannot be properly described here.

To substantiate the relationship between the spectral shifts and electron and lattice temperatures, we conduct fluence-dependent measurements at these two time delays. The resulting spectral shifts from fitted spectra at > 36.5 eV depend linearly on pump fluence [Fig. 2(c)], indicating that the spectral shifts also depend linearly on the electron temperature and phonon populations. Potential nonlinearities induced by the second-order phase transition at the thermal transition threshold with corresponding pump fluence of 1.8 mJ/cm^2 (see Appendix C for more details) are not observed. This agrees with the negligible discontinuity of the derivative of the specific heat near the transition threshold [50]. In conclusion, the redshift is found to be a good measure of the thermal electron and phonon excitation. In this regard, it is justified to compare TDDFT calculations that omit CDW effects. In the temperature and fluence range explored in this study, we find that the nonlinearities arising from the temperature-dependent electronic and lattice specific heat are below the experimental sensitivity. The integration of the specific heat [50] reveals a deviation of less than 5% of the fluence-dependent temperature from a linear scaling. In addition, calculations at different electron temperatures confirm a linear dependence of the spectral shift on the electron temperature in the relevant fluence regime. In photoemission studies that offer a more detailed view on the electronic structure, it was shown that electron-electron scattering leads to a quasiequilibrium within the electron subsystem at a timescale of 200 fs [20]. In comparison, the spectral redshift is expected to be less sensitive to the finer details of the carrier distribution but serves as a good measure for the effective strength of electronic excitation, as indicated by the linear fluence dependence and the TDDFT calculations. As the *ab initio* simulations of lattice temperature effects are much more computationally intensive, comparison of simulation and experimentally measured spectra at 3-ps delay is beyond the scope of this work. However, we show that the spectrum at 3 ps is dominated by the lattice temperature contribution corresponding to a 30-K temperature increase, which is directly related to an increased electron temperature of 1000 K at 50 fs. Between 50 fs and 3 ps time delays, both electronic and lattice heating effects are present. Hence, by extracting the spectral shifts at each time delay, the time-dependent electron and lattice temperature can be qualitatively tracked. Figure 2(d) (red line) displays the fitted spectral shifts of the extended edge region as a function of the time delay. We fit the time-dependent redshift with two time constants (dashed lines) for the electronic (T_e) and phononic systems (T_b), which corresponds to a three-temperature model. In this model, a third system may store and exchange energy with the electrons and the phonon bath. The fitting yields a $T_e = 0.36 \pm 0.04$ ps decay and a $T_b = 1.0 \pm 0.3$ ps rise, which we assign as the electronic population decay time and phonon population rise time, respectively. A fit with a single time constant is incapable of describing the slight increase of the redshift between 1 and 3.3 ps and, more importantly, yields an unreasonable fast time constant of 280 fs for the lattice system which is expected to heat up on the 1 ps timescale [27].

B. Coherent phonon dynamics

The XUV transient absorption spectra exhibit oscillations as a function of the time delay [Fig. 1(c), right side] that stem from coherently excited lattice modes. In 1*T*-$TiSe_2$, harmonic orders 26–31 display oscillations at 3.3 and 6.0 THz as shown in Figs. 3(a), 3(b), 7, and 8. From phonon frequencies identified in previous Raman and optical pump-probe studies [26,51], the 6- and 3.3-THz oscillations are assigned to the A_{1g} optical mode and the A_{1g}^* CDW amplitude mode, respectively.

The optical mode consists of purely out-of-plane oscillations of all selenium atoms. In contrast, the amplitude mode, which involves the coherent oscillation of the PLD, comprises in-plane movements of both Ti and Se atoms. For comparison, the eigenvectors of these modes are depicted in Fig. 3(c). As the amplitude mode is found only in the PLD-ordered state below the critical temperature [51], a loss of its signal is interpreted as a partial suppression of the PLD order [26]. In this study, we observe a corresponding suppression of the amplitude mode by increasing the pump fluence from $F = 260\ \mu J/cm^2$ to $F = 660\ \mu J/cm^2$. At the higher fluence, the 3.3-THz signature is no longer discernible [HH 30, Figs. 3(a) and 3(b)], whereas the optical mode amplitude is largely unaffected.

Interestingly, the spectral changes induced by the two phonon modes are energy separated, and these spectral fingerprints are schematically drawn in Fig. 3(c). From the lineouts shown in Figs. 3(a) and 7 as well as their Fourier components displayed in Figs. 3(b) and 8, we identify three spectral regions with different contributions to the transient absorption signal. First, at photon energies below 38.7 eV (HH 25, green), no coherent oscillations are visible. Between 40.3 and 45 eV (red), the transient absorption spectra are dominated by the 6-THz oscillations assigned to the A_{1g} optical mode. Finally, the 3.3-THz oscillations corresponding to the amplitude mode appear only above 45 eV (blue).

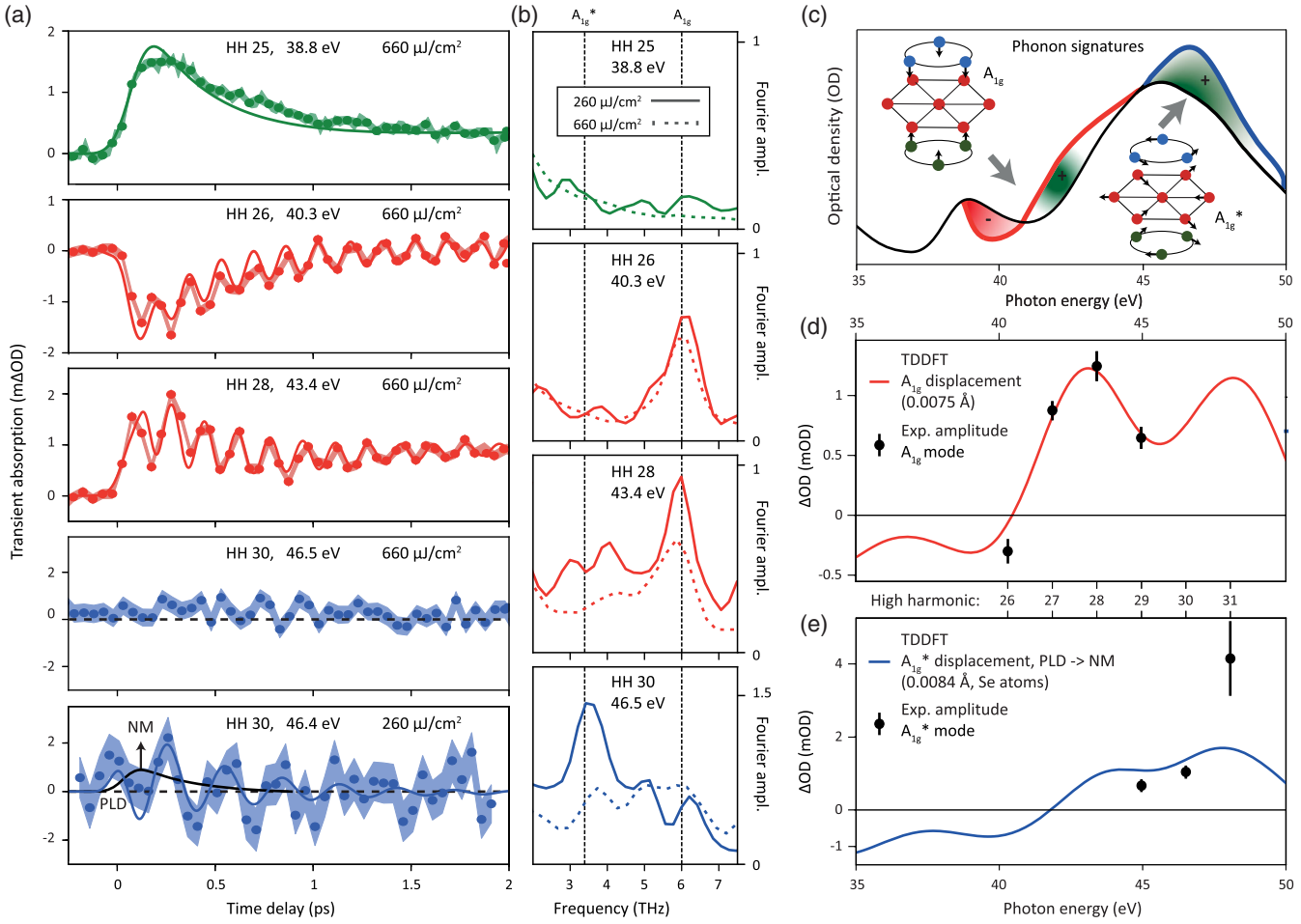

FIG. 3. (a) Selected transient absorption traces of $1T$-$TiSe_2$. Pump-probe traces are recorded for $F = 260\ \mu J/cm^2$ and $F = 660\ \mu J/cm^2$ at 110 K in the CDW phase. The sign of ΔOD is related to the direction of lattice displacement (see TDDFT calculations) and allows for assigning the displacements from the PLD to the high temperature, normal metallic (NM) state of $1T$-$TiSe_2$ for positive absorption changes at harmonic 30. (b) Fourier spectra of pump-probe traces. The observed 6- and 3-THz oscillations are attributed to the A_{1g} optical mode and the $A_{1g}{}^*$ amplitude mode of $1T$-$TiSe_2$. The optical mode is largely independent of the pump fluence, while the signature of the amplitude mode is suppressed at large excitation. (c) Schematic sketch of the phonon mode spectral fingerprints. The optical and the amplitude mode can be assigned to a characteristic change in the spectrum which are qualitatively illustrated here. (d) Spectral change of the A_{1g} displacement calculated by TDDFT compared to the initial oscillation amplitude in the pump-probe traces. (e) The same as (d) but for the $A_{1g}{}^*$ amplitude mode.

The spectral fingerprints of the observed oscillations are further analyzed by direct comparison with TDDFT calculations. Here, the spectra are computed for small atomic displacements along the phonon eigenmodes predicted by DFT simulations [52], which are schematically shown as black arrows in Fig. 3(c). By comparing the spectra to the absorption of an undistorted lattice, the expected change in the optical density is calculated (see Appendix E for more information). In Figs. 3(d) and 3(e), the calculated OD change is compared to the experimentally observed oscillation amplitude near time zero. The spectral fingerprints are well reproduced by the DFT model. The simulated ΔOD for the amplitude mode shows a maximum amplitude at the 31st harmonic and a smaller response at the 30th and 29th harmonics. A very different spectral response at harmonics 26–29 is observed for the optical mode. Here, the sign reversal between harmonics 26 and 27, which can also be seen by comparing HH 26 and HH 28 in Fig. 3(a), is faithfully reproduced by the calculations. At larger photon energies, the optical mode signal can no longer be clearly distinguished from the noise level despite being predicted by the simulations. This is due to the increased noise at the cutoff wavelength of our light source. Thus, potential signatures of the optical mode that could be seen in the Fourier spectra at harmonics 30 and 31 in Figs. 3(b) and 8 are not included in the above discussion.

With the link to real-space coordinates provided by the TDDFT calculations, the direction of the atomic movements related to positive or negative absorption changes can be unambiguously identified. For the amplitude mode,

positive absorption changes correspond to an atomic movement from the PLD toward the high-temperature, normal (semi)metallic (NM) phase. In the case of the optical mode, a positive transient absorption of harmonics 27–29 is indicative of a contraction movement like shown in Fig. 3(c).

Besides the qualitative agreement, a comparison of TDDFT data to the experiment allows us to quantify the initial amplitude of the coherent oscillations. For the optical mode, the experimental absorption change is reproduced by Se atoms displaced by 0.0075 Å and for the amplitude mode by reducing the PLD by 30% (0.0084 Å for Se atoms and 0.0255 Å for Ti atoms). The energy stored in the modes can, thus, be estimated from the real-space displacements and the phonon frequencies. Under the assumption of a homogeneous excitation over the entire sample region probed, stored energies per normal-phase unit cell (u.c.) of 0.65 and 0.8 meV/u.c. are obtained for the optical and amplitude mode near time zero, respectively (Appendix C). These values represent a significant fraction of the 260 $\mu J/cm^2$ pump fluence, which translates to an absorbed energy of 6 meV/u.c. (Appendix C). Interestingly, at the larger fluence of 660 $\mu J/cm^2$, the amplitude of the optical mode excitation remains largely unchanged compared to the low-fluence data, implying that the efficiency of phonon excitation is nonlinear. This is further discussed in Sec. III.

In order to obtain meaningful damping times of the coherent modes, we use a global fit that simultaneously fits a single oscillation with a frequency f and a common damping T_p to multiple harmonics (see Appendix D for details). Here, we use all harmonics that display either the optical or the amplitude mode to extract the intrinsic phonon dephasing times. Resulting fits are shown as solid lines in Figs. 3(a) and 7, and details of the fit parameters are described in Appendix D. The optical mode shows a dephasing time of $T_p = 1.3 \pm 0.5$ ps and $T_p = 1.0 \pm 0.2$ ps for the 260 and the 660 $\mu J/cm^2$ fluence measurement, respectively. For the amplitude mode, we extract a damping of $T_p = 0.6 \pm 0.2$ ps. We find that the obtained time constants of both phonon modes are in good agreement with previous studies [23]. In the global fit model, we exclude harmonic 26 from the global fit of the optical mode, as the phonon signature at this harmonic is strongly affected by the electron and lattice-induced redshift [Fig. 2(a)]. This leads to the seemingly stark difference between the strong damping of harmonic 28 and the weaker damping of harmonic 26 as shown in Fig. 3(a). We discuss the influence of the redshift on the measured damping times in more detail in Appendix D and Fig. 6.

While harmonic 30 does not show any contribution of an elevated electron temperature at the larger fluence of 660 $\mu J/cm^2$, the oscillation of the amplitude mode is found to be displaced to positive optical density changes within the first picosecond at 260 $\mu J/cm^2$ excitation [black line in Fig. 3(a)]. A similar behavior of an additional positive absorption change is visible at harmonic 29 in Fig. 7. We assign this component to an additional displaced atomic position. This short-lived positive absorption change can be associated with a mean displacement of the amplitude mode from the PLD state toward the high-temperature NM phase, in accordance with the TDDFT calculations. Such transient oscillation around a new equilibrium position may be associated to a displacive excitation mechanism that is expected for the amplitude mode in 1T-$TiSe_2$ [21,24]. However, usually the oscillation of displacive excitation occurs around a new equilibrium position and relaxes on larger timescales.

III. DISCUSSION

In this study, we spectrally separate coherent excitations of the A_{1g}^* amplitude mode and the simultaneously excited A_{1g} optical mode in 1T-$TiSe_2$. We find that only the amplitude mode is suppressed above a certain threshold fluence in agreement with the previously reported nonthermal CDW suppression [15,24,28,29]. For better comparison to previous experiments, the incident fluences used in this work ($F = 260$ $\mu J/cm^2$ and $F = 660$ $\mu J/cm^2$) are converted to deposited energy per unit cell (u.c.) (see Appendix C) resulting in 6 and 15 meV/u.c., respectively. At the lower excitation density of 6 meV/u.c., the amplitude mode is well visible and suppressed at 15 meV/u.c. deposited energy. Considering the stark differences in the experimental setup, sample, temperature, and pump wavelength, this threshold is still in reasonable agreement with the previously reported threshold value of 4 meV/u.c. [23]. Since the nonthermal melting of the CDW strongly depends on the exact electron excitation mechanism, different excitation configurations and especially different pump wavelengths lead to deviating threshold fluences. In conclusion, a comparison of absolute fluences and microscopic mechanisms between two separate experiments is often challenging. This highlights the value of simultaneous observations on electronic and phononic subsystems by the same probe, which facilitate a direct comparison. As the amplitude mode exists only in the PLD-ordered state, its suppression is a clear indication of a loss of PLD order. We estimate a temperature increase of approximately 30 K for the fluence of 0.66 mJ/cm^2, which is insufficient to drive the system above the transition temperature of 200 K. Nevertheless, this fluence still leads to a suppression of the PLD as indicated by the vanishing of the amplitude mode. Various mechanisms have been proposed to describe this nonthermal melting of 1T-$TiSe_2$, ranging from exciton breaking to a loss of 3D coherence [15,24,28,29].

To gain more insights into the mechanism of CDW excitations in 1*T*-$TiSe_2$, understanding the photoinduced dynamics and the interplay of the electronic and phononic systems is of great importance. The spectral redshift is found to qualitatively track electronic and lattice heating. An effect of the CDW or PLD melting on the spectral shift is not observed. This is confirmed by the linear fluence dependence, shown at 50 fs and 3 ps pump-probe delays in Fig. 2. Additionally, we find that the signal from the optical mode persists independent of the fluence, and we do not observe any direct involvement of the optical mode on the quenching of the CDW or PLD state. The observed nonlinear dependence of the excitation efficiency on the fluence is consistent with previous work. A sublinear scaling has been reported above the threshold [23], and our work extends this observation to lower fluences. A possible mechanism could be the indirect influence of the nonlinearly excited electronic system which determines the excitation efficiency of the phonon mode. While the optical mode's spectral fingerprint resides near the absorption edge, the spectral region of the amplitude mode coincides with the many-body absorption peak. As the many-body resonance results from local dynamic screening effects, we find strong evidence of a coupling of the amplitude mode to a perturbation of the electronic screening and cooperative electron motion [37,53]. Specifically, coherent excitations of the amplitude mode, associated with the PLD, lead to an altered electronic screening at the Ti atoms, which is reflected by the spectral changes in the many-body peak. This result supports an interplay of electron-electron interactions and electron-phonon coupling for the CDW stability in light of the ongoing discussion regarding the CDW driving mechanism in 1*T*-$TiSe_2$ [7–14]. Conversely, a perturbed electron-electron correlation may be one cause of the amplitude mode excitation. However, it should be noted that, while our results provide important insights into the interplay between electron-electron interactions and electron-phonon coupling in the stability of the CDW in 1*T*-$TiSe_2$, a complete understanding of the relative contributions of excitonic and electron-phonon coupling mechanisms to the CDW transition requires further investigation. Therefore, future studies should aim to explore the exact nature of the excitonic or electron-phonon coupling and their roles in the CDW transition of 1*T*-$TiSe_2$. Additionally, we find weak implications of a displacive phonon excitation. It describes the mechanism of an instantaneous change in the atomic potential landscape after electronic excitation, which leads to a motion toward a new equilibrium structure. The cosine phase that is often used as indication of displacive excitation cannot be applied in this study, as such phase assignments are beyond the sensitivity of our probe. However, we observe that the optically excited electronic system drives the atoms toward the normal metallic state. For displacive excitations, the system oscillates around the new equilibrium position before slowly relaxing back [54]. In this study, we find a very weak displacement toward the normal metallic state of 1*T*-$TiSe_2$ which decays within the first picosecond. Such a fast relaxation is unusual for displacive excitation and may hint at a more complex excitation pathway that warrants further investigation.

At larger timescales in the picosecond regime, energy transfer between the phonon modes drastically influences the dynamics. Both the optical mode and the amplitude mode are strongly excited and transiently store a significant fraction of the excitation energy, which is redistributed on their respective damping timescales. We find that 11% of the 6 meV/u.c. excitation ($F = 260\ \mu J/cm^2$) are initially deposited in the optical mode, while 14% are transferred to the amplitude mode. The effect of transient energy storage in the phonon modes can be seen when comparing the extracted timescales. The lattice heats up significantly slower on the 1-ps timescale compared to the cooling of the electronic system, which occurs on roughly 360 fs. In this regard, we find evidence of a bottleneck effect that hinders the heating of the lattice due to the transient energy which is stored in hot phonon modes. After laser irradiation, coherent modulations of the A_{1g} and A_{1g}^* modes are triggered together with electronic excitation. The electron subsystem relaxes on the approximately 300 fs timescale while further exciting incoherent populations of strongly coupled phonon modes [23], to which the A_{1g} and the A_{1g}^* mode also belong. These hot phonons store a significant amount of energy that is redistributed on a timescale close to or larger than the 1-ps dephasing time measured in this study.

IV. CONCLUSION

In this work, we use high-sensitivity transient absorption spectroscopy with a HHG source to investigate and distinguish various electronic and lattice contributions of the weakly excited CDW in 1*T*-$TiSe_2$. Thereby, we paid particular attention to the coherently excited phonon modes. The out-of-plane A_{1g} optical phonon can be separated from the $A_{1g}{}^*$ amplitude mode, as each mode hosts a specific spectral fingerprint. We find that the amplitude mode signature is rooted in the many-body absorption peak of the static absorption spectrum, indicating that an excited $A_{1g}{}^*$ mode strongly changes the local electron screening. These results closely link the CDW amplitude mode to the many-body screening which is dominated by the local electron density around the Ti core. In a reciprocal manner, a perturbation of the electron-electron correlation may, therefore, be the cause of the amplitude mode excitation. Using TDDFT, the spectral fingerprints can be reproduced and linked to real-space lattice displacements. With the knowledge of displacements

and frequencies, the deposited energies and the excitation efficiencies of the two modes are thus estimated. In this work, the unique sensitivity of XUV absorption spectroscopy allows us to simultaneously measure the excitation efficiency of the A_{1g} out-of-plane oscillations and the A_{1g}^{*} in-plane CDW mode. Complementary analysis of spectral shifts enables simultaneous extraction of the timescales of electronic cooling and phonon-bath heating on the same dataset. This allows us to obtain a more refined picture of the energy relaxation in 1T-$TiSe_2$, where the heating of the lattice is delayed due to excitations of strongly coupled hot phonons.

This work exemplifies the potential of high-sensitivity transient absorption spectroscopy for the investigation of quantum materials by simultaneously probing electronic and lattice degrees of freedom. A simultaneous sensitivity to the presented degrees of freedom by other means is extremely challenging. In future experiments, our approach may be combined with spectrally continuous sources to enable simultaneous access to coherent phonon dynamics and detailed information on electron and hole interactions on attosecond timescales [47]. The extracted spectral fingerprints of the phonon modes may prove valuable in further experiments, such as imaging with high-harmonic sources. In addition, the presented approach may be applied to a variety of phenomena with strongly coupled dynamics of electronic and lattice systems like CDW formation, metal-to-insulator transitions, and superconductivity.

ACKNOWLEDGMENTS

This work was funded with resources from the Gottfried Wilhelm Leibniz Prize and the Deutsche Forschungsgesellschaft (DFG). We thank Stephen R. Leone for providing lab instruments to record continuous XUV spectra of 1T-$TiSe_2$, which was funded by the Air Force Office of Scientific Research (FA9550-19-1-0314 and FA9550-20-1-0334). H.-T. C. acknowledges support from Air Force Office of Scientific Research (FA9550-19-1-0314 and FA9550-20-1-0334) and Alexander von Humboldt Foundation. The simulations were conducted at the Scientific Compute Cluster at GWDG, the joint data center of Max Planck Society for the Advancement of Science (MPG) and University of Göttingen.

APPENDIX A: SAMPLE PREPARATION

This study uses 1T-$TiSe_2$ flakes grown by chemical vapor transport [55] and cut to $L = 65$ nm thickness at lateral sizes of approximately 300 μm by ultramicrotomy. The flakes are positioned on a commercial TEM membrane of 30-nm-thick nanocrystalline, porous silicon (SiMPore) consisting of eight 100×100 μm and one $350\ \mu m \times 100\ \mu m$ windows. By aligning the sample with the windows, some are fully covered while others remain empty to allow for absolute transmission measurements compared to the pure silicon transmission. A schematic sample is depicted in Fig. 4(a).

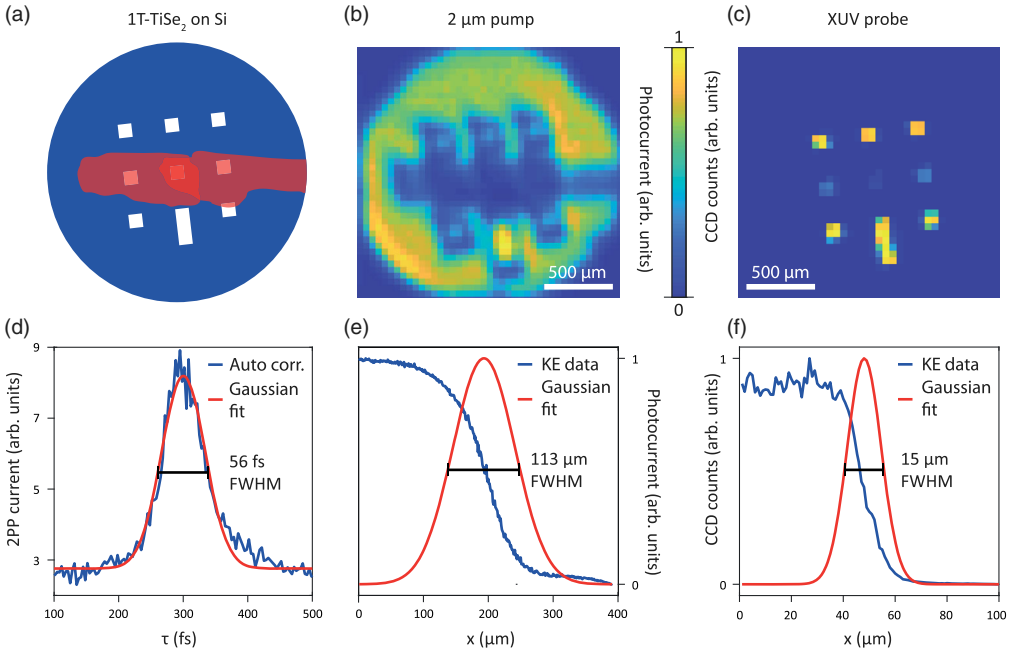

FIG. 4. (a) Schematic of nine window Si membrane apertures and a 1T-$TiSe_2$ flake positioned on top. (b),(c) Transmitted intensity of pump and probe beam used for spatial overlapping of both beams. (d) Intensity autocorrelation of the pump pulse recorded by two-photon absorption. (e),(f) Knife-edge (KE) measurements of pump and probe beam and estimated Gaussian beam profile.

APPENDIX B: TRANSIENT ABSORPTION SETUP

Infrared-pump XUV-probe core-level transient absorption measurements are carried out with a tabletop high-harmonic source [Figs. 1(a) and 5]. It is driven by a 1-kHz Ti:sapphire 35-fs laser amplifier with a central wavelength of 800 nm and generates XUV radiation with spectral range of 25–50 eV in an Ar-filled gas cell. The high-harmonic spectrum comprises peaks with 1.55 eV spacing, achieved by a bicolor laser excitation scheme [56]. It consists of a β-barium borate (BBO) crystal to generate the second harmonic and two calcite plates to adjust the temporal overlap with respect to the fundamental pulse. The sample is excited by a 2-μm laser pulse with 40-fs pulse duration and an incidence angle of 5° generated in an optical parametric amplifier (OPA). The wavelength is chosen to achieve a homogeneous absorption profile in the depth of the sample. Our setup consists of two toroidal gratings that spectrally disperse the XUV beam before the sample and after transmission through the sample. The two spectra, referred to as the reference and signal spectrum, are simultaneously detected on a charge-coupled device (CCD) camera. In combination with feed-forward neural network fitting [33], this procedure achieves a sensitivity of $< 10^{-4}$ OD. Pump-probe traces are recorded with alternating pumped and unpumped frames and randomly distributed timing delays, to avoid systematic drifts in time. By evaluating the spot sizes on the detector, we estimate a spectral width of approximately 250 meV (FWHM) for the harmonics as an upper limit, given the aberration broadening of the optical system.

Spatial overlap of pump and probe beams is achieved by scanning the sample in the focal plane and obtaining the position of the pump and probe beams through maps of the transmitted intensity. Two example transmission maps are shown in Figs. 4(b) and 4(c). The integrated CCD counts and photocurrent of an additional infrared photodiode placed in the transmitted pump beam path measure the transmittance. In addition, these scans can be used for knife-edge measurements to estimate the probe and pump beam sizes on the sample as shown in Figs. 4(e) and 4(f). The spot profiles are analyzed by Gaussian fits to estimate spot diameters of $d_{\mathrm{pump}} = 113$ μm and $d_{\mathrm{probe}} = 15$ μm for pump and probe beam at full width at half maximum (FWHM), respectively. These dimensions are chosen such that the probe can be positioned well within the 100-μm windows while ensuring homogeneous excitation by the pump beam.

To estimate the temporal resolution, the pump and probe pulse durations and the wavefront tilt originating from the noncollinear excitation are considered. By utilizing two-photon photoabsorption in a conventional silicon diode, intensity autocorrelation is performed on the 2-μm pump pulse. An autocorrelation width of $\tau_{\mathrm{a.c.}} = 56$ fs is extracted by fitting a Gaussian pulse shape as shown in Fig. 4(d). The resulting pulse length of $\tau_{\mathrm{pump}} = \tau_{\mathrm{a.c.}}/\sqrt{2} = 40$ fs is significantly larger than the expected $\tau_{\mathrm{XUV}} \approx 10$ fs pulse length of the XUV beam [57]. An additional contribution stems from the 5° pulse front tilt between pump and probe pulses. This additional temporal shear over the probed length of $d = 15$ μm can be computed by $\tau_{\mathrm{tilt}} = d_{\mathrm{probe}} \times \sin(5°)/c$ (c is the speed of light) and is found to be 4.5 fs. The combined temporal resolution is governed by the pump pulse width and is estimated to be 41 fs by convolution.

APPENDIX C: ABSORBED ENERGY

With the assumption of a Gaussian spot profile and nearly collinear excitation, the incident fluence is calculated as

$$F = P/(f \times r_{\mathrm{pump}}^2 \times \pi). \tag{C1}$$

Here, the $1/e$ radius of the pump pulse $r_{\mathrm{pump}} = d_{\mathrm{pump}}/[2\sqrt{\ln(2)}]$, the laser repetition rate f, and the

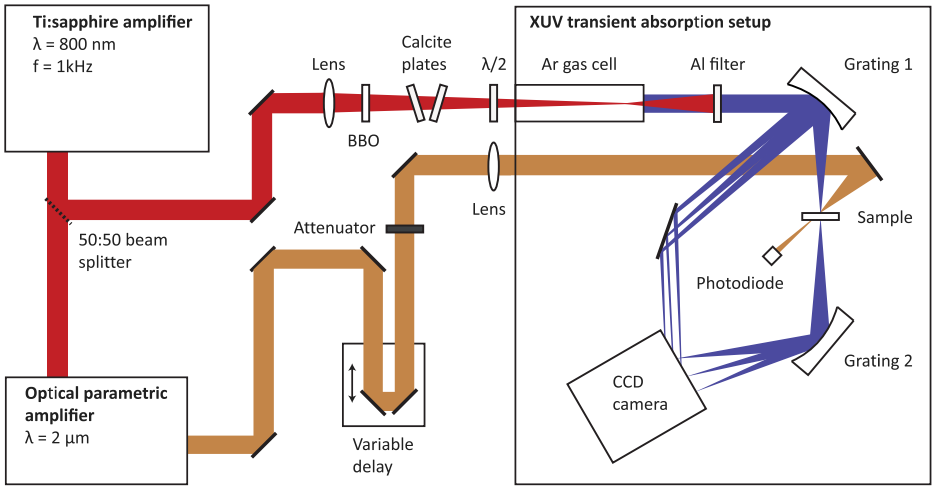

FIG. 5. Schematic of the transient absorption setup.

measured pump power P are used. Furthermore, the absorbed fluence can be estimated by subtracting reflected and transmitted portions for samples of length L:

$$F_{\mathrm{abs}} = F \times (1-R) \times [1 - e^{-L/\delta} \times (1-R)]. \quad \text{(C2)}$$

From the literature, a reflectivity of $R = 60\%$ (Ref. [58]) and an absorption length of $\delta = 41$ nm (Ref. [58]) are used for the 2-μm pump wavelength. To obtain an accurate measure of the excitation density, the absorbed fluence is converted to deposited energy per Ti atom (normal state unit cell) by

$$E_{\mathrm{u.c.}} = F_{\mathrm{abs}}/(L \times \rho), \quad \text{(C3)}$$

with the atomic density $\rho = 1.536 \times 10^{22}$ u.c./cm^3 (Ref. [59]). However, for reflection studies on bulk samples, the formalism needs to be adjusted. Specifically, the length L is set to half of the probe attenuation depth, and a second reflection is omitted. Table I compares the incident fluence and absorbed energy of this work to selected literature values. Under the assumption of homogeneous excitation and full equilibration, the expected temperature increase due to laser excitation is calculated by integrating the known heat capacity [50]. For the temperature increase from 110 K to the equilibrium phase transition temperature of 200 K, we find a fluence of 1.8 mJ/cm^2. By contrast, the fluence of 660 μJ/cm^2 leads to a temperature increase of roughly 30 K, which cannot drive the CDW melting through a thermal mechanism.

A significant portion of the absorbed energy is initially stored in the coherently excited phonon modes $A_{1g}{}^*$ and A_{1g}. From the TDDFT calculation, the maximal elongation from the equilibrium position x_i of the atoms (i = Ti, Se) can be estimated, which allows one to calculate the potential energy for a specific phonon mode in the spring model by

$$E = 0.5 \times \sum_i \alpha_i \omega^2 x_i^2 M_i. \quad \text{(C4)}$$

Here, ω is the phonon oscillation frequency, M_i is the atomic mass of the atom, and α_i is the number of moving atoms per normal phase unit cell. For the A_{1g} optical mode, both Se atoms ($\alpha_{\mathrm{Se}} = 2$, $\alpha_{\mathrm{Ti}} = 0$) in the unit cell are displaced by $x_{\mathrm{Se}} = 0.0075$ Å. In the case of the amplitude mode $A_{1g}{}^*$, we use $\alpha_{\mathrm{Se}} = \frac{6}{4}$, $\alpha_{\mathrm{Ti}} = \frac{3}{4}$, $x_{\mathrm{Se}} = 0.0084$ Å, and $x_{\mathrm{Ti}} = 0.0255$ Å, since only a fraction of the atoms participate in the mode. This leads to an energy of $E = 0.65$ meV/u.c. and $E = 0.8$ meV/u.c., stored in the coherently excited amplitude of the A_{1g} and the $A_{1g}{}^*$ mode, respectively. Incoherent excitations of the modes are not captured here, and the total stored energy might be even larger. For the calculation, the excitation is assumed to be homogeneous over the sample, such that each unit cell is equally excited.

TABLE I. Excitation fluences and deposited energy per unit cell normalized to the probed sample volume.

Dataset	Fluence F (μJ/cm^2)	Energy $E_{\mathrm{u.c.}}$ (meV)
This work	260, 660	5.9, 15.0
Hedeyat *et al.* [23]	62	4.0

APPENDIX D: FITTING PROCEDURE

Phonon damping timescales are extracted by global fits with the equation

$$\begin{aligned}\Delta\mathrm{OD}(\tau) = {} & 0.5 \times \left[\mathrm{erf}\left(\frac{\tau}{T_{r1}}\right) + 1\right] \times \left\{A_e \times \exp\left(-\frac{\tau}{T_e}\right) + A_b \times \left[1 - \exp\left(-\frac{\tau}{T_b}\right)\right]\right\} \\ & + 0.5 \times \left[\mathrm{erf}\left(\frac{\tau}{T_{r2}}\right) + 1\right] \times A_p \times \sin(2\pi f \tau + \phi) \times \exp\left(-\frac{\tau}{T_p}\right). \end{aligned} \quad \text{(D1)}$$

Here, T_{r1} and T_{r2} represent the rise times after excitation, A_e, A_b, and A_p the amplitude of the electron, phonon bath, and coherent phonon contributions, and T_e, T_b, and T_p the corresponding damping times, respectively. The values of $T_e = 0.36 \pm 0.04$ ps and $T_b = 1.0 \pm 0.3$ ps are taken from the result of the time-dependent spectral redshift [Fig. 2(c)], as these time constants should be independent of the harmonic order. We distinguish the rise times of the electronic T_{r1} and phononic system T_{r2} to incorporate the different physical excitation mechanisms which exceed the duration of the pump pulse. For the extraction of phonon dephasing times, we use a global fit incorporating all harmonics that show a signature of the individual phonon mode. Here, a single phonon oscillation at frequency f, its associated phase ϕ, and damping constant T_p are fit to multiple harmonics in a single fitting. Only the amplitudes are allowed to vary between different wavelengths. For the amplitude mode ($F = 260$ μJ/cm^2) harmonics 29–31 are utilized, while for the optical mode the fit includes harmonic 27 and 28. At $F = 660$ μJ/cm^2, harmonics 27–29 are used in the fitting. The fittings are displayed in Figs. 3(a) and 7, and the fitting parameters for

TABLE II. Fitting parameters of the global fit for the A_{1g} and A_{1g}^{*} phonon modes.

Phonon	Fluence	Harmonics	T_{r1} (fs)	T_{r2} (fs)	f (THz)	ϕ	T_p (ps)
A_{1g}^{*}	260 μJ/cm^2	29, 30, 31	⋯	90 ± 70	3.4 ± 0.1	3.4 ± 0.3	0.6 ± 0.2
A_{1g}	260 μJ/cm^2	27, 28	100 ± 30	50 ± 50	5.9 ± 0.1	0.7 ± 0.2	1.3 ± 0.5
A_{1g}	660 μJ/cm^2	27, 28, 29	80 ± 10	60 ± 50	6.0 ± 0.1	0.8 ± 0.2	1.0 ± 0.2

both phonon modes are shown in Table II for both fluences. Since the time zero is not independently known, the phase is used as a time-zero offset and cannot directly be used to extract a cosine behavior indicative of displacive excitation.

In the global fit, harmonic 26 is neglected, as it is significantly modulated by the redshift leading to a much larger damping time. A separate fit of this harmonic reveals a damping time of 2.3 ± 0.5 ps, which is significantly larger than the 1 ps extracted by the global fit. The modulation of the apparent phonon amplitude by a redshift is schematically shown in Fig. 6. The black curve indicates the expected phonon signature of the A_{1g} optical mode. A redshift of this spectral fingerprint (red lines) leads to a significant reduction of the amplitude at harmonic 26 and minor changes at larger photon energies, indicated by the arrows. The modulation is particularly strong at harmonic 26, as it is situated near the maximal slope and the zero crossing of the phonon spectral signature. As shown in Fig. 2(d), the redshift induced by electronic and lattice heating is strongly time dependent, which affects the observed phonon amplitude and damping at harmonic 26. Specifically, a large redshift near time zero reduces the observed amplitude. However, during the initial decay of the redshift on the timescale of 360 fs, the observed phonon amplitude is artificially increased, leading to an overestimation of the phonon damping time. Afterward, the redshift is constant and the apparent phonon relaxation thus remains unaltered. Therefore, the influence of the redshift on the observed timescales can be significant near the zero crossing as shown in the case of harmonic 26. However, in the spectral region of harmonics 27–29, a global fit can be safely used to extract the phonon damping timescale.

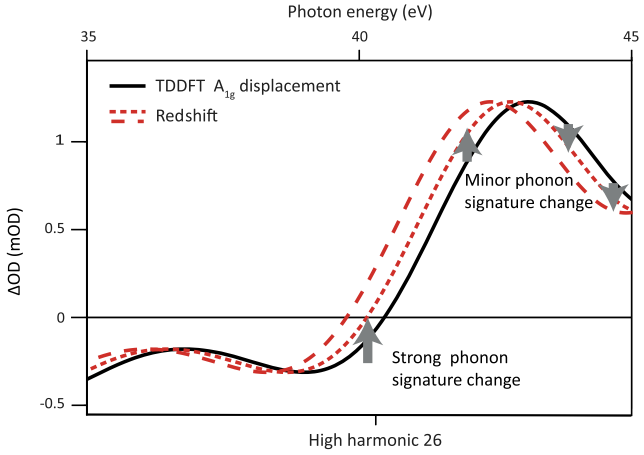

FIG. 6. Schematic illustration of the influence of the spectral shift on the optical mode signature. At a given probe energy, the redshifted spectral signature can increase or decrease the visible phonon signal. The apparent signal at harmonic 26 is strongly reduced by a redshift, as it is situated near the maximal slope and the zero crossing of the phonon signature. At larger photon energies, in the plateau region of the phonon fingerprint the effects of the redshift are only minor.

APPENDIX E: SIMULATIONS OF XUV SPECTRA WITH TIME-DEPENDENT DENSITY FUNCTIONAL THEORY

The Ti $M_{2,3}$-edge absorption spectra in Figs. 1(b), 2(b), 3(d), and 3(e) are simulated with TDDFT in the random phase approximation and the full-potential linearized augmented plane wave method using the *exciting* software package [60–62]. We employ the framework of TDDFT in the linear response theory to capture the dynamical core-level excitation process that leads to the absorption of XUV radiation. The calculations are performed with a Perdew-Burke-Ernzerhof exchange-correlation functional [63], and local field effects are included in all TDDFT calculations to incorporate the effects of many-body interactions on the core-level absorption [35,38,64]. Spectral calculations with atomic displacements along the A_{1g} optical mode are conducted with a single unit cell on a $12 \times 12 \times 6$ k grid. Equilibrium atomic positions are obtained via geometry optimization by relaxing the structure and minimizing internal forces with initial atomic positions taken from Ref. [65]. The atomic displacements of the optical mode are taken from subsequent phonon calculations at the Γ point. Simulations of the core-level absorption spectra with displacements along the amplitude mode are conducted with a $2 \times 2 \times 2$ supercell. The atomic positions for the CDW and normal phase are taken from Ref. [52]. Here, the ground state DFT calculations are first carried out on a $12 \times 12 \times 6$ k grid, and the following TDDFT spectral simulations are conducted on a $6 \times 6 \times 3$ k grid. Simulations at increased electron temperature are conducted by adjusting the electron occupation with the Fermi distributions at finite temperature in the calculation of the density [66]. As a result, the calculated electronic bands as well as the occupation account for the increased electron temperature.

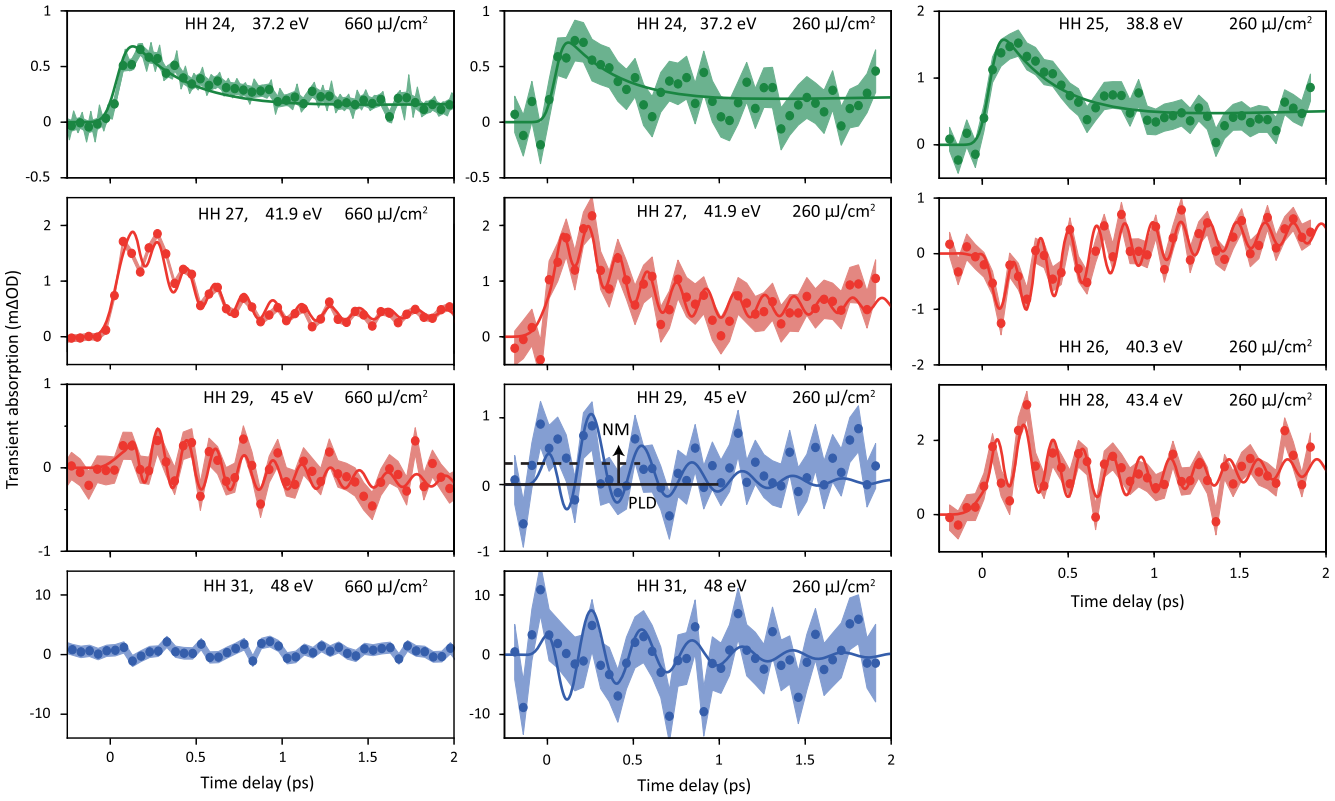

FIG. 7. Transient absorption traces of $1T$-$TiSe_2$. Pump probe traces are recorded for $F = 260\ \mu J/cm^2$ and $F = 660\ \mu J/cm^2$.

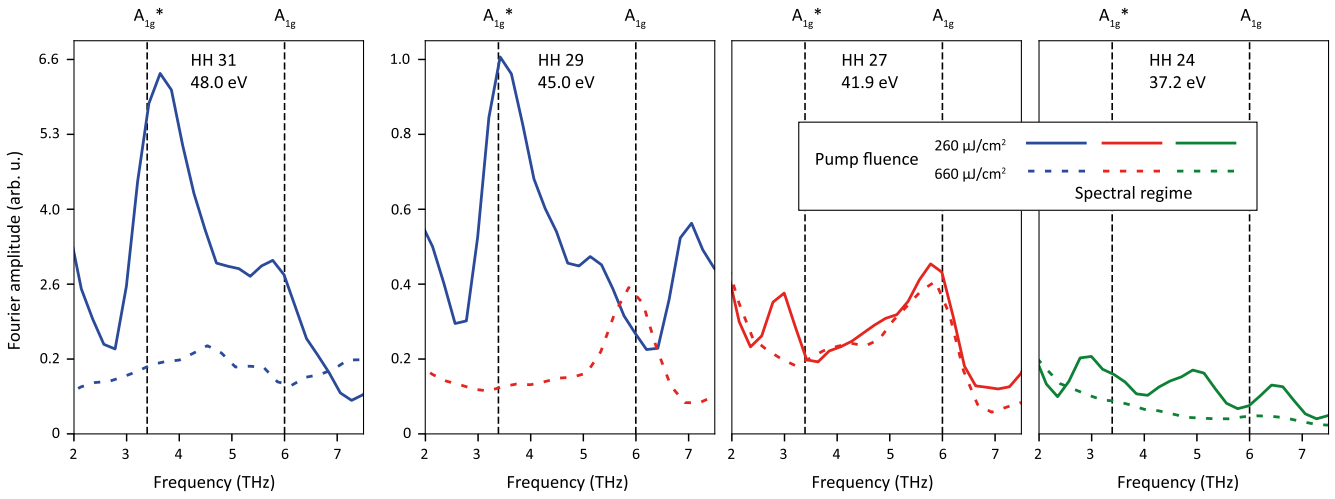

FIG. 8. Fourier spectra of pump-probe traces.

[1] G. Grüner, *Density Waves in Solids*, Frontiers in Physics Vol. 89 (Addison-Wesley, Advanced Book Program, Reading, MA, 1994).

[2] M. Imada, A. Fujimori, and Y. Tokura, *Metal-Insulator Transitions*, Rev. Mod. Phys. **70**, 1039 (1998).

[3] E. Dagotto, *Complexity in Strongly Correlated Electronic Systems*, Science **309**, 257 (2005).

[4] D. N. Basov, R. D. Averitt, D. van der Marel, M. Dressel, and K. Haule, *Electrodynamics of Correlated Electron Materials*, Rev. Mod. Phys. **83**, 471 (2011).

[5] F. J. Di Salvo, D. E. Moncton, and J. V. Waszczak, *Electronic Properties and Superlattice Formation in the Semimetal* $TiSe_2$, Phys. Rev. B **14**, 4321 (1976).

[6] K. C. Woo, F. C. Brown, W. L. McMillan, R. J. Miller, M. J. Schaffman, and M. P. Sears, *Superlattice Formation in Titanium Diselenide*, Phys. Rev. B **14**, 3242 (1976).

[7] H. P. Hughes, *Structural Distortion in* $TiSe_2$ *and Related Materials-a Possible Jahn-Teller Effect?*, J. Phys. C **10**, L319 (1977).

[8] M. H. Whangbo and E. Canadell, *Analogies between the Concepts of Molecular Chemistry and Solid-State Physics Concerning Structural Instabilities. Electronic Origin of the Structural Modulations in Layered Transition Metal Dichalcogenides*, J. Am. Chem. Soc. **114**, 9587 (1992).

[9] K. Rossnagel, L. Kipp, and M. Skibowski, *Charge-Density-Wave Phase Transition in* $1T - TiSe_2$*: Excitonic Insulator versus Band-type Jahn-Teller Mechanism*, Phys. Rev. B **65**, 235101 (2002).

[10] J. van Wezel, P. Nahai-Williamson, and S. S. Saxena, *Exciton-Phonon-Driven Charge Density Wave in* $TiSe_2$, Phys. Rev. B **81**, 165109 (2010).

[11] H. Cercellier, C. Monney, F. Clerc, C. Battaglia, L. Despont, M. G. Garnier, H. Beck, P. Aebi, L. Patthey, H. Berger, and L. Forró, *Evidence for an Excitonic Insulator Phase in* $1T - TiSe_2$, Phys. Rev. Lett. **99**, 146403 (2007).

[12] C. Monney, E. F. Schwier, M. G. Garnier, N. Mariotti, C. Didiot, H. Cercellier, J. Marcus, H. Berger, A. N. Titov, H. Beck, and P. Aebi, *Probing the Exciton Condensate Phase in* $1T$-$TiSe_2$ *with Photoemission*, New J. Phys. **12**, 125019 (2010).

[13] A. Kogar, M. S. Rak, S. Vig, A. A. Husain, F. Flicker, Y. I. Joe, L. Venema, G. J. MacDougall, T. C. Chiang, E. Fradkin, J. van Wezel, and P. Abbamonte, *Signatures of Exciton Condensation in a Transition Metal Dichalcogenide*, Science **358**, 1314 (2017).

[14] K. Rossnagel, *On the Origin of Charge-Density Waves in Select Layered Transition-Metal Dichalcogenides*, J. Phys. Condens. Matter **23**, 213001 (2011).

[15] E. Möhr-Vorobeva, S. L. Johnson, P. Beaud, U. Staub, R. De Souza, C. Milne, G. Ingold, J. Demsar, H. Schaefer, and A. Titov, *Nonthermal Melting of a Charge Density Wave in* $TiSe_2$, Phys. Rev. Lett. **107**, 036403 (2011).

[16] M. Huber, Y. Lin, N. Dale, R. Sailus, S. Tongay, R. A. Kaindl, and A. Lanzara, *Mapping the Dispersion of the Occupied and Unoccupied Band Structure in Photoexcited* $1T$-$TiSe_2$, J. Phys. Chem. Solids **168**, 110740 (2022).

[17] T. Rohwer, S. Hellmann, M. Wiesenmayer, C. Sohrt, A. Stange, B. Slomski, A. Carr, Y. Liu, L. M. Avila, M. Kalläne, S. Mathias, L. Kipp, K. Rossnagel, and M. Bauer, *Collapse of Long-Range Charge Order Tracked by Time-Resolved Photoemission at High Momenta*, Nature (London) **471**, 490 (2011).

[18] F. Weber, S. Rosenkranz, J.-P. Castellan, R. Osborn, G. Karapetrov, R. Hott, R. Heid, K.-P. Bohnen, and A. Alatas, *Electron-Phonon Coupling and the Soft Phonon Mode in* $TiSe_2$, Phys. Rev. Lett. **107**, 266401 (2011).

[19] S. Hellmann, T. Rohwer, M. Kalläne, K. Hanff, C. Sohrt, A. Stange, A. Carr, M. M. Murnane, H. C. Kapteyn, L. Kipp, M. Bauer, and K. Rossnagel, *Time-Domain Classification of Charge-Density-Wave Insulators*, Nat. Commun. **3**, 1069 (2012).

[20] S. Mathias, S. Eich, J. Urbancic, S. Michael, A. V. Carr, S. Emmerich, A. Stange, T. Popmintchev, T. Rohwer, M. Wiesenmayer, A. Ruffing, S. Jakobs, S. Hellmann, P. Matyba, C. Chen, L. Kipp, M. Bauer, H. C. Kapteyn, H. C. Schneider, K. Rossnagel, M. M. Murnane, and M. Aeschlimann, *Self-Amplified Photo-Induced Gap Quenching in a Correlated Electron Material*, Nat. Commun. **7**, 12902 (2016).

[21] C. Monney, M. Puppin, C. W. Nicholson, M. Hoesch, R. T. Chapman, E. Springate, H. Berger, A. Magrez, C. Cacho, R. Ernstorfer, and M. Wolf, *Revealing the role of electrons and phonons in the ultrafast recovery of charge density wave correlations in* $1T$-$TiSe_2$, Phys. Rev. B **94**, 165165 (2016).

[22] T. E. Karam, J. Hu, and G. A. Blake, *Strongly Coupled Electron–Phonon Dynamics in Few-Layer* $TiSe_2$ *Exfoliates*, ACS Photonics **5**, 1228 (2018).

[23] H. Hedayat, C. J. Sayers, D. Bugini, C. Dallera, D. Wolverson, T. Batten, S. Karbassi, S. Friedemann, G. Cerullo, J. van Wezel, S. R. Clark, E. Carpene, and E. Da Como, *Excitonic and Lattice Contributions to the Charge Density Wave in* $1T$-$TiSe_2$ *Revealed by a Phonon Bottleneck*, Phys. Rev. Res. **1**, 023029 (2019).

[24] M. Burian, M. Porer, J. R. L. Mardegan, V. Esposito, S. Parchenko, B. Burganov, N. Gurung, M. Ramakrishnan, V. Scagnoli, H. Ueda, S. Francoual, F. Fabrizi, Y. Tanaka, T. Togashi, Y. Kubota, M. Yabashi, K. Rossnagel, S. L. Johnson, and U. Staub, *Structural Involvement in the Melting of the Charge Density Wave in* $1T$-$TiSe_2$, Phys. Rev. Res. **3**, 013128 (2021).

[25] S. Duan, Y. Cheng, W. Xia, Y. Yang, C. Xu, F. Qi, C. Huang, T. Tang, Y. Guo, W. Luo, D. Qian, D. Xiang, J. Zhang, and W. Zhang, *Optical Manipulation of Electronic Dimensionality in a Quantum Material*, Nature (London) **595**, 239 (2021).

[26] H. Hedayat, C. J. Sayers, A. Ceraso, J. van Wezel, S. R. Clark, C. Dallera, G. Cerullo, E. Da Como, and E. Carpene, *Investigation of the Non-Equilibrium State of Strongly Correlated Materials by Complementary Ultrafast Spectroscopy Techniques*, New J. Phys. **23**, 033025 (2021).

[27] M. R. Otto, J.-H. Pöhls, L. P. René de Cotret, M. J. Stern, M. Sutton, and B. J. Siwick, *Mechanisms of Electron-Phonon Coupling Unraveled in Momentum and Time: The Case of Soft Phonons in* $TiSe_2$, Sci. Adv. **7**, eabf2810 (2021).

[28] M. Porer, U. Leierseder, J.-M. Ménard, H. Dachraoui, L. Mouchliadis, I. E. Perakis, U. Heinzmann, J. Demsar, K. Rossnagel, and R. Huber, *Non-Thermal Separation of Electronic and Structural Orders in a Persisting Charge Density Wave*, Nat. Mater. **13**, 857 (2014).

[29] Y. Cheng, A. Zong, J. Li, W. Xia, S. Duan, W. Zhao, Y. Li, F. Qi, J. Wu, L. Zhao, P. Zhu, X. Zou, T. Jiang, Y. Guo, L. Yang, D. Qian, W. Zhang, A. Kogar, M. W. Zuerch, D. Xiang, and J. Zhang, *Light-Induced Dimension Crossover Dictated by Excitonic Correlations*, Nat. Commun. **13**, 963 (2022).

[30] H.-T. Chang, A. Guggenmos, C. T. Chen, J. Oh, R. Géneaux, Y.-D. Chuang, A. M. Schwartzberg, S. Aloni, D. M.

Neumark, and S. R. Leone, *Coupled Valence Carrier and Core-Exciton Dynamics in* WS_2 *Probed by Few-Femtosecond Extreme Ultraviolet Transient Absorption Spectroscopy*, Phys. Rev. B **104**, 064309 (2021).

[31] A. R. Attar, H.-T. Chang, A. Britz, X. Zhang, M.-F. Lin, A. Krishnamoorthy, T. Linker, D. Fritz, D. M. Neumark, R. K. Kalia, A. Nakano, P. Ajayan, P. Vashishta, U. Bergmann, and S. R. Leone, *Simultaneous Observation of Carrier-Specific Redistribution and Coherent Lattice Dynamics in* $2H$-$MoTe_2$ *with Femtosecond Core-Level Spectroscopy*, ACS Nano **14**, 15829 (2020).

[32] T. P. H. Sidiropoulos, N. Di Palo, D. E. Rivas, S. Severino, M. Reduzzi, B. Nandy, B. Bauerhenne, S. Krylow, T. Vasileiadis, T. Danz, P. Elliott, S. Sharma, K. Dewhurst, C. Ropers, Y. Joly, M. E. Garcia, M. Wolf, R. Ernstorfer, and J. Biegert, *Probing the Energy Conversion Pathways between Light, Carriers, and Lattice in Real Time with Attosecond Core-Level Spectroscopy*, Phys. Rev. X **11**, 041060 (2021).

[33] T. Heinrich, H.-T. Chang, S. Zayko, M. Sivis, and C. Ropers, *High-Sensitivity Extreme-Ultraviolet Transient Absorption Spectroscopy Enabled by Machine Learning*, arXiv:2305.02236.

[34] G.-J. Shu, Y. Zhou, M.-Y. Kao, C. J. Klingshirn, M. R. S. Huang, Y.-L. Huang, Y. Liang, W. C. H. Kuo, and S.-C. Liou, *Investigation of the* π *Plasmon and Plasmon-Exciton Coupling in Titanium Diselenide (*$TiSe_2$*) by Momentum-Resolved Electron Energy Loss Spectroscopy*, Appl. Phys. Lett. **114**, 202103 (2019).

[35] E. E. Krasovskii and W. Schattke, *Local Field Effects in Optical Excitations of Semicore Electrons*, Phys. Rev. B **60**, R16251 (1999).

[36] *Giant Resonances in Atoms, Molecules, and Solids*, NATO ASI Series Vol. 151, edited by J. P. Connerade, J. M. Esteva, and R. C. Karnatak (Springer, Boston, 1987).

[37] M. Y. Amusia and J.-P. Connerade, *The Theory of Collective Motion Probed by Light*, Rep. Prog. Phys. **63**, 41 (2000).

[38] M. Volkov, S. A. Sato, F. Schlaepfer, L. Kasmi, N. Hartmann, M. Lucchini, L. Gallmann, A. Rubio, and U. Keller, *Attosecond Screening Dynamics Mediated by Electron Localization in Transition Metals*, Nat. Phys. **15**, 1145 (2019).

[39] Z. Schumacher, S. A. Sato, S. Neb, A. Niedermayr, L. Gallmann, A. Rubio, and U. Keller, *Ultrafast Electron Localization and Screening in a Transition Metal Dichalcogenide*, arXiv:2210.05465.

[40] M. Zürch, H.-T. Chang, L. J. Borja, P. M. Kraus, S. K. Cushing, A. Gandman, C. J. Kaplan, M. H. Oh, J. S. Prell, D. Prendergast, C. D. Pemmaraju, D. M. Neumark, and S. R. Leone, *Direct and Simultaneous Observation of Ultrafast Electron and Hole Dynamics in Germanium*, Nat. Commun. **8**, 15734 (2017).

[41] M. Zürch, H.-T. Chang, P. M. Kraus, S. K. Cushing, L. J. Borja, A. Gandman, C. J. Kaplan, M. H. Oh, J. S. Prell, D. Prendergast, C. D. Pemmaraju, D. M. Neumark, and S. R. Leone, *Ultrafast Carrier Thermalization and Trapping in Silicon-Germanium Alloy Probed by Extreme Ultraviolet Transient Absorption Spectroscopy*, Struct. Dynam. **4**, 044029 (2017).

[42] F. Schlaepfer, M. Lucchini, S. A. Sato, M. Volkov, L. Kasmi, N. Hartmann, A. Rubio, L. Gallmann, and U. Keller, *Attosecond Optical-Field-Enhanced Carrier Injection into the* GaAs *Conduction Band*, Nat. Phys. **14**, 560 (2018).

[43] M.-F. Lin, M. A. Verkamp, J. Leveillee, E. S. Ryland, K. Benke, K. Zhang, C. Weninger, X. Shen, R. Li, D. Fritz, U. Bergmann, X. Wang, A. Schleife, and J. Vura-Weis, *Carrier-Specific Femtosecond XUV Transient Absorption of* PbI_2 *Reveals Ultrafast Nonradiative Recombination*, J. Phys. Chem. C **121**, 27886 (2017).

[44] M. Verkamp, J. Leveillee, A. Sharma, M.-F. Lin, A. Schleife, and J. Vura-Weis, *Carrier-Specific Hot Phonon Bottleneck in* $CH_3NH_3PbI_3$ *Revealed by Femtosecond XUV Absorption*, J. Am. Chem. Soc. **143**, 20176 (2021).

[45] H.-T. Chang, A. Guggenmos, S. K. Cushing, Y. Cui, N. U. Din, S. R. Acharya, I. J. Porter, U. Kleineberg, V. Turkowski, T. S. Rahman, D. M. Neumark, and S. R. Leone, *Electron Thermalization and Relaxation in Laser-Heated Nickel by Few-Femtosecond Core-Level Transient Absorption Spectroscopy*, Phys. Rev. B **103**, 064305 (2021).

[46] E. Bévillon, J. P. Colombier, V. Recoules, and R. Stoian, *Free-Electron Properties of Metals under Ultrafast Laser-Induced Electron-Phonon Nonequilibrium: A First-Principles Study*, Phys. Rev. B **89**, 115117 (2014).

[47] M. Schultze, K. Ramasesha, C. D. Pemmaraju, S. A. Sato, D. Whitmore, A. Gandman, J. S. Prell, L. J. Borja, D. Prendergast, K. Yabana, D. M. Neumark, and S. R. Leone, *Attosecond Band-Gap Dynamics in Silicon*, Science **346**, 1348 (2014).

[48] S. K. Cushing, M. Zürch, P. M. Kraus, L. M. Carneiro, A. Lee, H.-T. Chang, C. J. Kaplan, and S. R. Leone, *Hot Phonon and Carrier Relaxation in* Si(100) *Determined by Transient Extreme Ultraviolet Spectroscopy*, Struct. Dynam. **5**, 054302 (2018).

[49] S. K. Cushing, A. Lee, I. J. Porter, L. M. Carneiro, H.-T. Chang, M. Zürch, and S. R. Leone, *Differentiating Photoexcited Carrier and Phonon Dynamics in the* Δ, L, *and* Γ *Valleys of* Si(100) *with Transient Extreme Ultraviolet Spectroscopy*, J. Phys. Chem. C **123**, 3343 (2019).

[50] R. Craven, F. Di Salvo, and F. Hsu, *Mechanisms for the* 200 K *Transition in* $TiSe_2$*: A Measurement of the Specific Heat*, Solid State Commun. **25**, 39 (1978).

[51] J. A. Holy, K. C. Woo, M. V. Klein, and F. C. Brown, *Raman and Infrared Studies of Superlattice Formation in* $TiSe_2$, Phys. Rev. B **16**, 3628 (1977).

[52] R. Bianco, M. Calandra, and F. Mauri, *Electronic and Vibrational Properties of* $TiSe_2$ *in the Charge-Density-Wave Phase from First Principles*, Phys. Rev. B **92**, 094107 (2015).

[53] A. L. Ankudinov, A. I. Nesvizhskii, and J. J. Rehr, *Dynamic Screening Effects in X-Ray Absorption Spectra*, Phys. Rev. B **67**, 115120 (2003).

[54] H. J. Zeiger, J. Vidal, T. K. Cheng, E. P. Ippen, G. Dresselhaus, and M. S. Dresselhaus, *Theory for Displacive Excitation of Coherent Phonons*, Phys. Rev. B **45**, 768 (1992).

[55] J. Wang, H. Zheng, G. Xu, L. Sun, D. Hu, Z. Lu, L. Liu, J. Zheng, C. Tao, and L. Jiao, *Controlled Synthesis of Two-Dimensional* $1T$-$TiSe_2$ *with Charge Density Wave*

Transition by Chemical Vapor Transport, J. Am. Chem. Soc. **138**, 16216 (2016).

[56] O. Kfir, E. Bordo, G. Ilan Haham, O. Lahav, A. Fleischer, and O. Cohen, *In-Line Production of a Bi-Circular Field for Generation of Helically Polarized High-Order Harmonics*, Appl. Phys. Lett. **108**, 211106 (2016).

[57] H. Igarashi, A. Makida, M. Ito, and T. Sekikawa, *Pulse Compression of Phase-Matched High Harmonic Pulses from a Time-Delay Compensated Monochromator*, Opt. Express **20**, 3725 (2012).

[58] S. C. Bayliss and W. Y. Liang, *Reflectivity, Joint Density of States and Band Structure of Group IVb Transition-Metal Dichalcogenides*, J. Phys. C **18**, 3327 (1985).

[59] C. Riekel, *Structure Refinement of* $TiSe_2$ *by Neutron Diffraction*, J. Solid State Chem. **17**, 389 (1976).

[60] A. Gulans, S. Kontur, C. Meisenbichler, D. Nabok, P. Pavone, S. Rigamonti, S. Sagmeister, U. Werner, and C. Draxl, *Exciting: A Full-Potential All-Electron Package Implementing Density-Functional Theory and Many-Body Perturbation Theory*, J. Phys. Condens. Matter **26**, 363202 (2014).

[61] C. Vorwerk, B. Aurich, C. Cocchi, and C. Draxl, *Bethe–Salpeter Equation for Absorption and Scattering Spectroscopy: Implementation in the Exciting Code*, Electro. Struct. **1**, 037001 (2019).

[62] S. Sagmeister and C. Ambrosch-Draxl, *Time-Dependent Density Functional Theory versus Bethe–Salpeter Equation: An All-Electron Study*, Phys. Chem. Chem. Phys. **11**, 4451 (2009).

[63] J. P. Perdew, K. Burke, and M. Ernzerhof, *Generalized Gradient Approximation Made Simple*, Phys. Rev. Lett. **77**, 3865 (1996).

[64] F. Aryasetiawan, O. Gunnarsson, M. Knupfer, and J. Fink, *Local-Field Effects in* NiO *and* Ni, Phys. Rev. B **50**, 7311 (1994).

[65] K. Persson, *Materials data on* $TiSe_2$ $(SG:164)$ *by Materials Project*, 2016.

[66] S. A. Sato, Y. Shinohara, T. Otobe, and K. Yabana, *Dielectric Response of Laser-Excited Silicon at Finite Electron Temperature*, Phys. Rev. B **90**, 174303 (2014).